Nonlinear Infragravity–Wave Interactions on a Gently Sloping Laboratory Beach

A. T. M. DE BAKKER

Faculty of Geosciences, Department of Physical Geography, Utrecht University, Utrecht, Netherlands

T. H. C. HERBERS AND P. B. SMIT

Theiss Research, La Jolla, California

M. F. S. TISSIER

Faculty of Civil Engineering and Geosciences, Environmental Fluid Mechanics Section, Delft University of Technology, Delft, Netherlands

B. G. RUESSINK

Faculty of Geosciences, Department of Physical Geography, Utrecht University, Utrecht, Netherlands

(Manuscript received 9 September 2014, in final form 13 November 2014)

ABSTRACT

A high-resolution dataset of three irregular wave conditions collected on a gently sloping laboratory beach is analyzed to study nonlinear energy transfers involving infragravity frequencies. This study uses bispectral analysis to identify the dominant, nonlinear interactions and estimate energy transfers to investigate energy flows within the spectra. Energy flows are identified by dividing transfers into four types of triad interactions, with triads including one, two, or three infragravity–frequency components, and triad interactions solely between short-wave frequencies. In the shoaling zone, the energy transfers are generally from the spectral peak to its higher harmonics and to infragravity frequencies. While receiving net energy, infragravity waves participate in interactions that spread energy of the short-wave peaks to adjacent frequencies, thereby creating a broader energy spectrum. In the short-wave surf zone, infragravity–infragravity interactions develop, and close to shore, they dominate the interactions. Nonlinear energy fluxes are compared to gradients in total energy flux and are observed to balance nearly completely. Overall, energy losses at both infragravity and short-wave frequencies can largely be explained by a cascade of nonlinear energy transfers to high frequencies (say, $f > 1.5$ Hz) where the energy is presumably dissipated. Infragravity–infragravity interactions seem to induce higher harmonics that allow for shape transformation of the infragravity wave to asymmetric. The largest decrease in infragravity wave height occurs close to the shore, where infragravity–infragravity interactions dominate and where the infragravity wave is asymmetric, suggesting wave breaking to be the dominant mechanism of infragravity wave dissipation.

1. Introduction

When short (2–20 s) ocean surface waves travel to shore, their shape transforms from (nearly) sinusoidal into skewed with peaked crests and flat troughs. In shallow water the wave shape becomes asymmetric with increasingly pitched forward crests that ultimately break in the surf zone. These shape transformations take place because of energy transfers between three wave components, often referred to as nonlinear triad interactions (Elgar and Guza 1985). Through such interactions energy is initially transferred from pairs of wave components (frequencies f_1 and f_2) near the dominant spectral peak f_p to higher frequencies by sum interactions ($f_1 + f_2 = f_3$); typically, $f_1 \approx f_2 \approx f_p$ and $f_3 \approx 2f_p$. Closer to the shore energy is also transferred to higher harmonics of f_p. Coincident with the shape transformation of the incident ocean waves, difference interactions ($f_1 - f_2 = f_3$)

Corresponding author address: A. T. M. de Bakker, Faculty of Geosciences, Department of Physical Geography, Utrecht University, Heidelberglaan 2, Room ZON 212, 3584 CS, Utrecht, Netherlands.
E-mail: a.t.m.debakker@uu.nl

DOI: 10.1175/JPO-D-14-0186.1

© 2015 American Meteorological Society

also transfer energy to infragravity waves (e.g., Herbers et al. 1994). Infragravity waves, longer (20–200 s) period waves, may be important for the erosion of beaches (e.g., Russell 1993) and dunes (Van Thiel de Vries et al. 2008) during storms. They are bound to the short-wave groups with a 180° phase difference (Longuet-Higgins and Stewart 1962), and have the same wave period and wavelength as the group. During the breaking of the short waves, the coupling between the short-wave group and the infragravity waves disappears (e.g., Ruessink 1998). The infragravity waves then propagate toward the beach as free waves and generally reflect from the shoreline to form cross-shore standing waves (e.g., Guza and Thornton 1982).

Studies on nonlinear interactions have thus far concentrated mostly on the short-wave frequency band of the energy spectrum. The offshore wave conditions, such as wave height, peak period, and directional spread, together with the local water depth and beach shape have been observed to influence the strength, direction, and involved frequency range of energy transfers within a wave field (e.g., Hasselmann et al. 1963; Elgar and Guza 1985; Herbers et al. 1994; Herbers and Burton 1997; Norheim et al. 1998). Although these variables are known to influence interactions including infragravity wave frequencies as well (e.g., Elgar and Guza 1985; Herbers et al. 1995; Norheim et al. 1998), overall interactions involving infragravity wave frequencies have received considerably less attention than interactions involving short-wave frequencies.

In recent years, a number of studies including field (e.g., Ruessink 1998; Sheremet et al. 2002; Henderson et al. 2006; Sénéchal et al. 2011; Guedes et al. 2013; De Bakker et al. 2014) and laboratory experiments (e.g., Battjes et al. 2004; Van Dongeren et al. 2007) as well as numerical modeling (Van Dongeren et al. 2007; Ruju et al. 2012) have shown that incoming infragravity waves can lose a considerable fraction of their energy close to shore. Henderson et al. (2006) and Thomson et al. (2006) attributed this energy loss to nonlinear energy transfers from infragravity frequencies back to short-wave frequencies and/or their higher harmonics. At their field sites, the beaches were steep to mild sloping (≈1:15 and 1:50, respectively), and infragravity energy levels were small compared to short-wave energy levels. Nonlinear interactions including infragravity frequencies were stronger during low tide when the beach shape was convex than during high tide when the beach shape was concave. These stronger interactions were probably because of the relatively longer time that the waves are in shallow water while propagating over a convex profile, compared to a concave profile (Thomson et al. 2006). Guedes et al. (2013) also observed nonlinear energy transfers from infragravity waves to higher frequencies ($f \approx 0.15$–0.5 Hz) on a gently sloping beach (≈1:70), where infragravity energy was much stronger. However, these transfers were too small to explain the large energy loss observed at infragravity frequencies in the near shore. Several other laboratory and field studies (Battjes et al. 2004; Van Dongeren et al. 2007; Lin and Hwung 2012; De Bakker et al. 2014) observed particularly large infragravity energy losses very close to the shoreline and ascribed it to the breaking of the infragravity waves themselves. This breaking was seen to be the consequence of infragravity–infragravity interactions that lead to the steepening of the infragravity waves and the development of "borelike" infragravity wave fronts, which become unstable and break. Ruju et al. (2012) suggested that both nonlinear energy transfers back to short waves and the breaking of the infragravity wave might each play a part in the observed infragravity wave energy dissipation. In the outer short-wave surf zone, where short-wave frequencies still dominate the water motion, the infragravity waves were predicted to transfer energy back to short waves through triad interactions. Close to the shoreline, the infragravity wave energy was predicted to dominate and be dissipated because of the steepening up of the infragravity wave by infragravity–infragravity interactions, causing the wave to become unstable and break. Despite all these research efforts, energy transfers and energy dissipation involving infragravity waves in the surf zone remain poorly understood.

In the present work, we analyze a high-resolution (both in space and time) dataset of irregular wave conditions collected on a small-scale, fixed, 1:80 laboratory beach and focus on nonlinear energy transfers involving infragravity frequencies. In section 2, we introduce our dataset and describe the bispectral analysis and nonlinear energy transfer equations. In section 3, we use bispectral analysis to demonstrate typical trends in the nonlinear interactions. More specifically, we investigate the dominant energy flows within the spectra by dividing the transfers into four different types of triad interactions, with triads including one, two, or three infragravity–frequency components and triad interactions solely between short-wave frequency components. In section 4, we compare the nonlinear energy fluxes with the gradients in total energy flux, discuss infragravity wave dissipation, and explore the similarities of our laboratory findings with recent field data from a gently sloping beach. We summarize the main findings in section 5.

2. Methods

a. *Laboratory experiments*

The laboratory dataset analyzed in this study was obtained during the Gently Sloping Beach Experiment

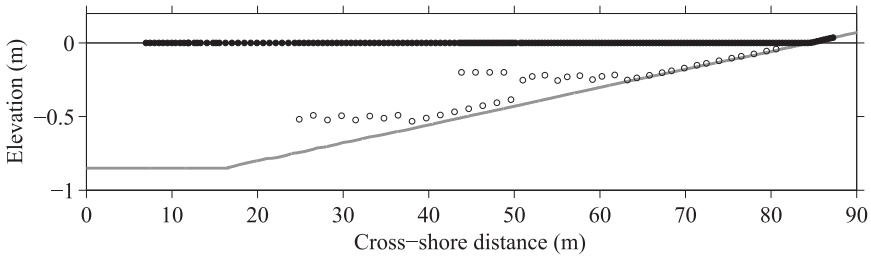

FIG. 1. Elevation z vs cross-shore distance x in the Scheldegoot during the GLOBEX project. Here, $x = 0$ is the location of the wave maker at rest, and $z = 0$ corresponds to the still water level. At $x = 84.6$ m, the still water level intersected with the bed. The 190 dots are the positions of the wave gauges, the 43 circles are the positions and heights above the bed of the electromagnetic current meters.

(GLOBEX) project (Ruessink et al. 2013). The experiments were performed in the Scheldegoot in Delft, the Netherlands, in April 2012. The flume is 110 m long, 1 m wide, and 1.2 m high and has a piston-type wave maker equipped with an active reflection compensation (ARC) to absorb waves coming from the flume and hence prevent their rereflection from the wave maker. A fixed, low-sloping (1:80) concrete beach was constructed over almost the entire length of the flume, except for the first 16.6 m that were horizontal and where the mean water level was 0.85 m (Fig. 1). At the cross-shore position $x = 16.6$ m ($x = 0$ m is the wave maker position at rest), the sloping bed started and intersected with the mean water level at $x \approx 84.6$ m. As detailed in Ruessink et al. (2013), the experimental program was composed of eight wave conditions. Here, we will focus on the three irregular wave cases: an intermediate energy sea wave condition ($A1$; $H_s = 0.1$ m; $T_p = 1.58$ s), a high energy sea wave condition ($A2$; $H_s = 0.2$ m; $T_p = 2.25$ s), and a narrowbanded swell condition ($A3$; $H_s = 0.1$ m; $T_p = 2.25$ s). All wave paddle steering signals included second-order wave generation (Van Leeuwen and Klopman 1996) and were based on a Joint North Sea Wave Project (JONSWAP) spectrum with a peak enhancement factor γ of 3.3 for $A1$ and $A2$ and 20 for $A3$. Each condition had a duration of 75 min with 21 wave gauges and five flow meters sampling at 128 Hz, followed by a rest period of about 15 min. After all wave conditions were completed, most instruments were repositioned and the conditions were repeated with the same wave paddle signal. Altogether, the conditions were each repeated 10 times, resulting in a total of 190 positions with water level η data and 43 positions with cross-shore flow velocity u data, with an instrument spacing varying from 2.2 m offshore to 0.55 m in the middle section and 0.37 m inshore (see Fig. 1). See Ruessink et al. (2013) for further details and initial data processing.

b. Dataset description

Figures 2a–c show the cross-shore evolution of the significant short-wave (Fig. 2a) and infragravity wave (Fig. 2b) heights for the three cases, together with the bottom profile (Fig. 2c). The separation frequencies f_{IG} of 0.37 ($A1$) and 0.26 Hz ($A2$ and $A3$) were chosen because the variance density spectra of η at the wave gauge closest to the wave maker contained a minimum at these frequencies. The significant wave height for both the short-wave H_{SW} and infragravity wave H_{IG} range was calculated as 4 times the standard deviation of the sea surface elevation of each frequency range. As can be seen, the short waves barely shoal and even decrease slightly in height for cases $A1$ and $A2$. Infragravity wave heights on the other hand increase considerably up to the outer edge of the short-wave surf zone, from whereon they stay constant or decrease slightly.

Figures 2d–f display the incoming and outgoing infragravity waves separately for the three conditions. The infragravity wave signals were separated in incoming and outgoing wave signals with the Guza et al. (1984) time-domain approach. This method uses collocated wave gauges and velocity meters to construct surface elevation time series of the incoming η^+ and outgoing η^- signals:

$$\eta^{\pm} = \frac{\eta \pm (h/g)^{1/2} u}{2}, \tag{1}$$

where h is water depth, and g is gravitational acceleration. The dependence of η on x here and in what follows is dropped for brevity. In Figs. 2d–f, the incoming wave heights are seen to increase until the edge of the short-wave surf zone, similar to the total infragravity wave signal. Further onshore the incoming wave heights decrease somewhat to increase again close to the shoreline (still water line is at $x \approx 84.6$ m). The substantial difference in incoming and outgoing infragravity wave height near the shoreline is striking and is indicative of strong infragravity energy dissipation in very shallow water (≈swash zone). The remaining outgoing infragravity waves decrease in height as they propagate offshore.

Figure 3 shows the infragravity energy fluxes and reflection coefficients. The incoming and outgoing

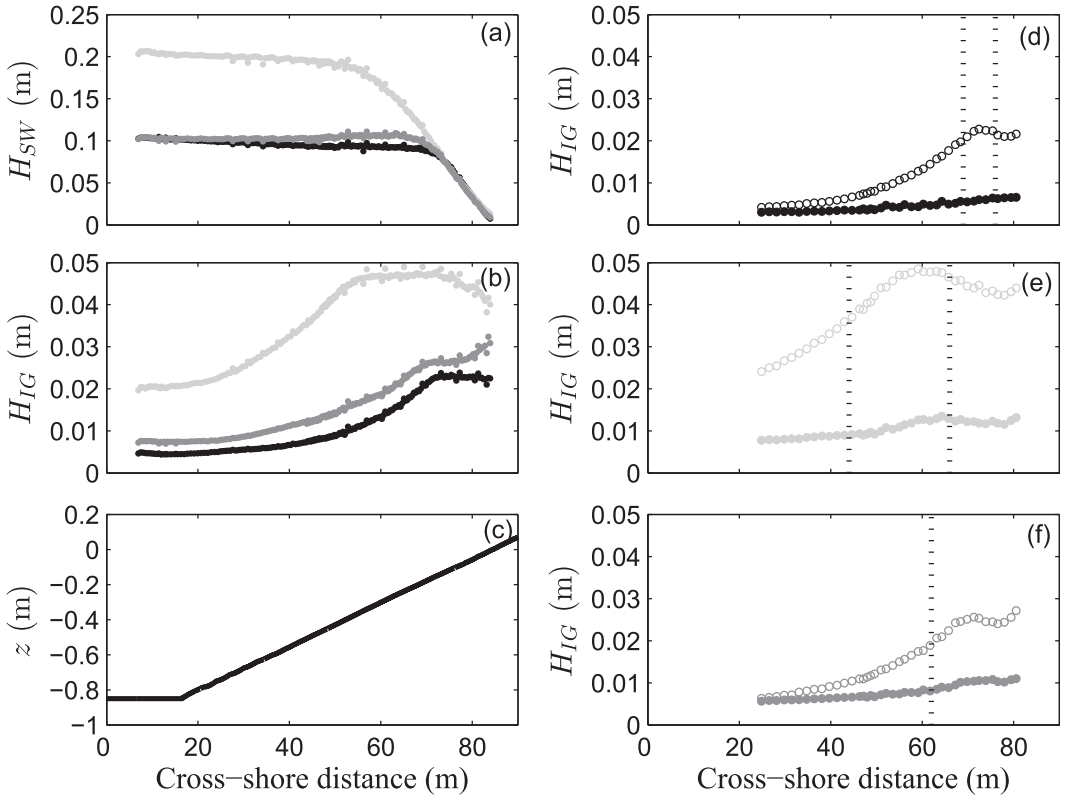

FIG. 2. Significant wave height vs cross-shore distance x for (a) short waves (H_{SW}) and (b) infragravity waves (H_{IG}) for $A1$ (black dots), $A2$ (light gray dots), and $A3$ (gray dots). (c) Bed profile. Furthermore, the significant incoming (circles) and outgoing (dots) infragravity wave heights calculated from separated signals (following Guza et al. 1984) are shown for (d) $A1$, (e) $A2$, and (f) $A3$. Visually observed locations where the highest waves started to break and the location from where all waves were observed to break were $x = 69$ and 76 m for $A1$ (indicated by vertical dashed lines), $x = 44$ and 66 m for $A2$, and just one location for $A3$, namely, $x = 62$ m, because of the narrowbanded spectral shape.

frequency-dependent energy fluxes F were determined with the spectral domain separation method of Sheremet et al. (2002):

$$F_f^{\pm} = N_f^{\pm}\sqrt{gh}, \tag{2}$$

$$N_f^{\pm} = \frac{1}{4}\left[C_{\eta\eta,f} + \frac{h}{g}C_{uu,f} \pm \left(2\sqrt{\frac{h}{g}}\right)C_{\eta u,f}\right], \tag{3}$$

where N is the energy, $C_{\eta u}$ is the $\eta - u$ cospectrum, and $C_{\eta\eta}$ and C_{uu} are η and u autospectra, respectively. Summation over infragravity frequencies gives the bulk infragravity energy flux $F_b^{\pm}$. The bulk reflection coefficient R_b^2 is defined as the ratio of the offshore to onshore propagating bulk infragravity energy flux $R_b^2 = F_b^-/F_b^+$. For all three conditions, the incoming infragravity energy fluxes increase up to the edge of the short-wave surf zone and then decrease considerably (Figs. 3a–c), varying from a decrease of about 50% for the intermediate energy sea case $A1$ and narrowbanded swell case $A3$ to about 65% for the high energy sea case $A2$. Almost all the remaining energy is dissipated either very close to the shoreline and/or in the swash zone, judging from the very low reflection coefficients of ≈0.1 (Figs. 3d–f).

c. Bispectral analysis

The bispectrum B_{f_1,f_2} detects the phase coupling between the frequency components in a triad. Here, we will introduce the bispectral analysis briefly; for a more in-depth description of bispectra, see, for example, Hasselmann et al. (1963) and Collis et al. (1998). The discrete bispectrum is defined as

$$B_{f_1,f_2} = E[A_{f_1}A_{f_2}A^*_{f_1+f_2}], \tag{4}$$

where $E[\,]$ is the ensemble average of the triple product of complex Fourier coefficients A at the frequencies f_1, f_2, and their sum $f_1 + f_2$, and the asterisk indicates complex conjugation. Likewise, the power spectrum is defined as

$$P_{f_1} = \frac{1}{2}E[A_{f_1}A^*_{f_1}]. \tag{5}$$

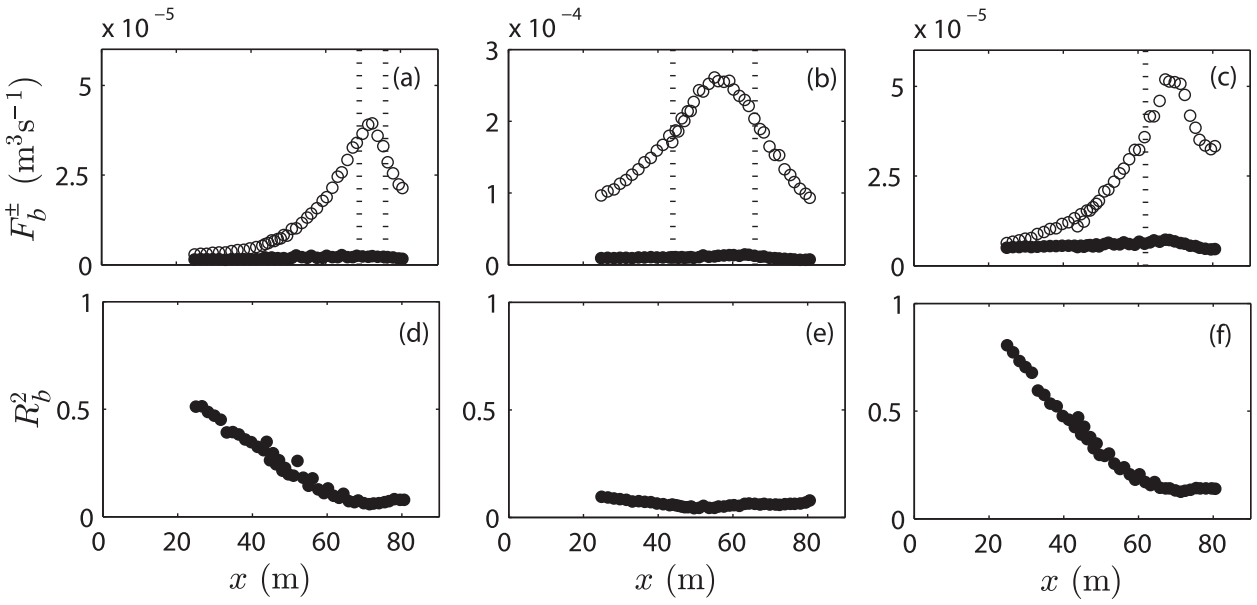

FIG. 3. Bulk incoming (F_b^+, circles) and outgoing (F_b^-, dots) infragravity energy fluxes vs cross-shore distance x for (a) $A1$, (b) $A2$, and (c) $A3$. Corresponding infragravity wave reflection coefficients R_b^2 vs cross-shore distance x for (d) $A1$, (e) $A2$, and (f) $A3$. Vertical dashed lines indicate visual breakpoint positions as specified in Fig. 2.

The normalized magnitude and phase of the bispectrum, called the bicoherence $b^2_{f_1,f_2}$ and biphase β_{f_1,f_2}, provide a normalized measure of the strength of the coupling and the phase relationship of the interacting wave components. They are here defined as

$$b^2_{f_1,f_2} = \frac{|B_{f_1,f_2}|^2}{P_{f_1} P_{f_2} P_{f_1+f_2}}, \tag{6}$$

and

$$\beta_{f_1,f_2} = \arctan\left(\frac{\mathrm{Im}\{B_{f_1,f_2}\}}{\mathrm{Re}\{B_{f_1,f_2}\}}\right), \tag{7}$$

following Collis et al. [1998, their Eq. (27)] and Kim and Powers (1979), where Im{ } and Re{ } are the imaginary and real part of the bispectrum, respectively. The stability of the biphase estimates is highly dependent on bicoherence values; for low bicoherence, the biphase is randomly distributed between π and $-\pi$. Although reflection from the shore was rather low for all three random wave cases (Figs. 3d–f); where possible, the incoming wave signal was used to avoid any reflection-related noise in the bispectral analysis (e.g., Elgar and Guza 1985). A comparison of the bispectra for the total and incoming wave signals is provided in appendix A.

d. Nonlinear energy transfers

Assuming the reflection from the shore to be small, the cross-shore energy flux gradient F_x on an alongshore uniform beach is balanced by the sum of a nonlinear source term S_{nl}, which accounts for energy transfers to and from a frequency f and a dissipation term S_{ds}, which accounts for wave breaking–induced energy losses and bottom friction (Herbers and Burton 1997; Herbers et al. 2000):

$$F_{x,f} = S_{\mathrm{nl},f} + S_{\mathrm{ds},f}. \tag{8}$$

In the case of flume experiments, side-wall friction may also be important. As we observed low reflection rates (Figs. 3d–f), Eq. (8) likely forms a reasonable approximation to the energy budget for our laboratory data. The energy flux gradient was determined from differences in the energy flux measured over the profile (dF/dx), where the energy flux (F_f) for each frequency is given by $P_f c_g$. Here, c_g is the group velocity. The nonlinear source term S_{nl} was estimated by integrating the product of the imaginary part of the surface elevation bispectrum B_{f_1,f_2} and a coupling coefficient. Various approximations of the coupling coefficient have been introduced, ranging from the Boussinesq scaling (e.g., Herbers and Burton 1997) valid for resonant waves in shallow water up to the more generalized theory (e.g., Janssen 2006), which includes full linear dispersive effects. In shallow water during both shoaling and breaking short-wave conditions, the Boussinesq approximation yields reliable results (Herbers and Burton 1997; Herbers et al. 2000; Smit et al. 2014). Using the stochastic formulation of the second-order nonlinear wave interaction theory of

Herbers et al. [2000, their Eq. (4)], S_{nl} can be determined discretely by

$$S_{\mathrm{nl},f} = \frac{3\pi f}{h}\,\mathrm{Im}\left\{\left(\sum_{f'=0}^{f} B_{f',f-f'} - 2\sum_{f'=0}^{\infty} B_{f',f}\right)\right\}, \qquad (9)$$

where the imaginary part of the bispectrum represents the energy transfers and is integrated in two parts. The term $\sum_{f'=0}^{f} B_{f',f-f'}$ accounts for the sum interactions in the bispectrum, and the term $-2\sum_{f'=0}^{\infty} B_{f',f}$ accounts for the difference interactions. Wave reflection is assumed negligible in the used Boussinesq approximation of Herbers and Burton (1997), although Henderson et al. (2006) showed that the reflection of infragravity waves does not invalidate the nonlinear source term approximations of Herbers and Burton (1997).

The estimate of the nonlinear source term as given by Eq. (9) includes the energy transfers by all possible interactions. To obtain better insight into the relative importance of interactions between infragravity waves and short waves, or between infragravity waves alone, we separated the interactions into four different categories with triads including either one, two, or three infragravity frequencies or triads including only interactions between short-wave frequencies. In the bispectrum, this separation can be visualized as four different zones (Fig. 4). The three involved frequencies (f_1, f_2, f_3) are depicted in the bispectral plane with f_1 along the horizontal axis, f_2 along the vertical axis, and f_3 as the sum of f_1 and f_2. In zone I, interactions include infragravity frequencies only, zone II involves two infragravity frequencies and one short-wave frequency, zone III includes one infragravity and two short-wave frequencies, and zone IV includes solely short-wave frequencies. The corresponding energy transfers can be obtained by integrating Eq. (9) over each of the bispectral zones; see appendix B for definitions. Arguably, this separation is somewhat arbitrary in that it depends on an artificially chosen upper limit to the infragravity band. Nevertheless, it is seen to be a useful method to identify the dominant energy flows within the spectrum.

e. Implementation

For the present bispectral analysis, the time series were resampled to 10 Hz and divided into blocks of 15 min (the total record length per simulation excluding the spinup at the start of the simulation was 69 min). Averaging of the bispectral estimates over 15 frequencies resulted in a frequency resolution of 0.0167 Hz and 240 degrees of freedom. The b^2 values larger than 0.158 are statistically significant from 0 at the 95% confidence level, based on the approximation of Kim and Powers (1979).

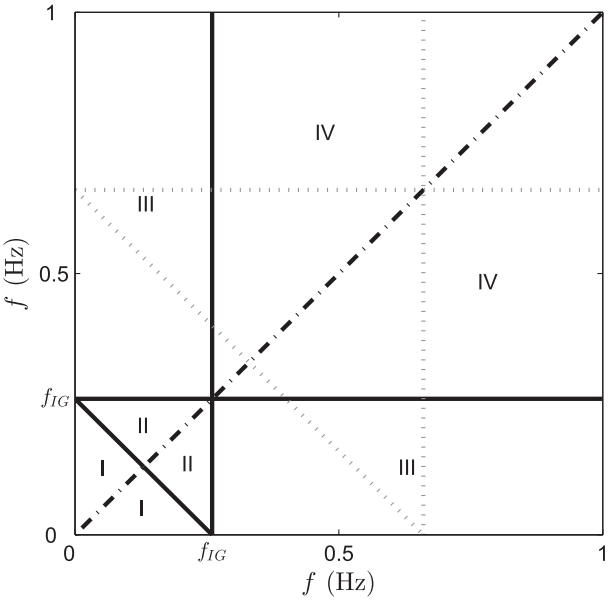

FIG. 4. Bispectrum separated into four zones by solid lines. Zone I contains infragravity frequencies only, zone II contains two infragravity and one short-wave frequency, zone III contains two short-wave and one infragravity frequency, and zone IV contains short-wave frequencies only. The present figure shows the case *A*3, with $f_{\mathrm{IG}} = 0.26$ Hz. The black dashed–dotted line indicates the symmetry of the bispectra. The gray dotted lines indicate the integration for an example frequency $f = 0.66$ Hz, consisting of three branches, a diagonal branch for sum interactions (S_{nl}^{+}), and horizontal and vertical branches for difference interactions (S_{nl}^{-}).

Biphases (β_{f_1,f_2}) were integrated over the infragravity (β_{IG}; zone I) and short-wave (β_{SW}; zone IV) frequency bands separately and combined ($\beta_{\mathrm{IG,SW}}$; zone II and III) as

$$\beta_{\mathrm{IG}} = \arctan\left(\frac{\mathrm{Im}\left\{\sum_{f_1=0}^{f_{\mathrm{IG}}}\sum_{f_2=0}^{f_{\mathrm{IG}}}\{B_{f_1,f_2}\}\right\}}{\mathrm{Re}\left\{\sum_{0}^{f_{\mathrm{IG}}}\sum_{0}^{f_{\mathrm{IG}}}\{B_{f_1,f_2}\}\right\}}\right), \qquad (10)$$

$$\beta_{\mathrm{SW}} = \arctan\left(\frac{\mathrm{Im}\left\{\sum_{f_1=f_{\mathrm{IG}}}^{2\mathrm{Hz}}\sum_{f_2=f_{\mathrm{IG}}}^{2\mathrm{Hz}}\{B_{f_1,f_2}\}\right\}}{\mathrm{Re}\left\{\sum_{f_1=f_{\mathrm{IG}}}^{2\mathrm{Hz}}\sum_{f_2=f_{\mathrm{IG}}}^{2\mathrm{Hz}}\{B_{f_1,f_2}\}\right\}}\right), \qquad (11)$$

and

$$\beta_{\mathrm{IG,SW}} = \arctan\left(\frac{\mathrm{Im}\left\{\sum_{f_1=f_{\mathrm{IG}}}^{2\mathrm{Hz}}\sum_{f_2=0}^{f_{\mathrm{IG}}}\{B_{f_1,f_2}\}\right\}}{\mathrm{Re}\left\{\sum_{f_1=f_{\mathrm{IG}}}^{2\mathrm{Hz}}\sum_{f_2=0}^{f_{\mathrm{IG}}}\{B_{f_1,f_2}\}\right\}}\right). \qquad (12)$$

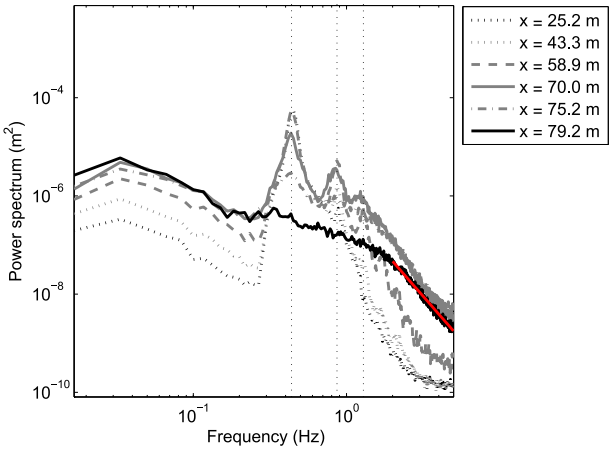

FIG. 5. Power spectra of the incoming wave signal during $A3$ at six cross-shore locations. The red line indicates the $f^{-3.6}$ dependence for the high-frequency tail of the spectrum (f = 2–5 Hz) at x = 79.2 m. The vertical dashed lines indicate the positions of the spectral peak (f = 0.44 Hz), the first harmonic (f = 0.88 Hz), and the second harmonic (f = 1.32 Hz).

To determine the cross-shore energy flux gradient F_x, rather than using occasionally noisy sensor-to-sensor estimates, we estimated F_x as the slope of a linear regression using all flux estimates in a cross-shore window with a width of twice the local wavelength of the offshore spectral peak frequency. This width varied between 5.7 and 1.0 m. On average, 16 points were used to determine the slope. The Boussinesq source term approximation used to determine the nonlinear energy transfers S_{nl} assumes that $kh \ll 1$, where k is the wavenumber. Although we are including rather high frequencies (up to ≈5 Hz) where this approximation is violated, the transfers in these off-resonant triad interactions are small, and their contribution to the integrals is negligible. For our analysis, we are mostly interested in the processes close to shore and in frequencies smaller than the first harmonic of the spectral peak ($f < 0.88$ Hz), where $kh < 1$.

3. Results

Figure 5 shows the power spectra for six cross-shore positions for case $A3$, from x = 25.2 m near the wave paddle to x = 79.2 m, very close to the shoreline. The results of case $A3$ are shown as this narrowbanded condition has clearly distinguishable peaks in the power and bispectrum. This facilitates interpretations of the results compared with the two other cases that are more broadbanded and where energy peaks and interactions are spread over more frequencies. At x = 25.2 m, a clear peak at f = 0.44 Hz is present. In the shoaling zone, the energy levels at the spectral peak stay more or less the same, but additional peaks develop due to nonlinear interactions; one at the first harmonic (f = 0.88 Hz), and one at infragravity frequencies (f = 0.04 Hz). In the first part of the short-wave surf zone (x = 70.0 m), the spectral peak decreases strongly, while the secondary peaks continue to develop. The energy around the spectral peak and the first harmonic are seen to shift slightly to lower frequencies. Deep into the surf zone (x = 75.2 m) the first harmonic decreases as well, while the infragravity peak develops further. Very close to the shoreline (x = 79.2 m), the infragravity frequencies dominate the spectrum. Here, the high-frequency spectral tail of the spectrum (f = 2–5 Hz) has a $f^{-3.6}$ rolloff, typical of saturation (Thornton 1979).

The imaginary part of the bispectra at those same six locations is shown in Fig. 6. Colors indicate the direction of the energy transfers, and color intensity is a proxy of the magnitude of the energy transfers (for absolute transfers the bispectral values need to be multiplied with the interaction coefficient). Positive values at B_{f_1,f_2} indicate a transfer from f_1 and f_2 to f_3, the sum frequency. Negative values indicate a transfer from f_3 to f_1 and f_2. Figure 6a shows that close to the wave maker triad interactions are dominated by a positive interaction around B(0.44, 0.44), which is the peak–peak interaction transferring energy to the first harmonic at f_3 = 0.88 Hz, and a negative interaction near B(0.42, 0.04), with energy transfers from f_3 = 0.46 Hz to both f_1 = 0.42 Hz and f_2 = 0.04 Hz. This last interaction causes the energy around the spectral peak to shift slightly to lower frequencies as seen in Fig. 5 (at, e.g., x = 70 m) and generates infragravity energy. Up to the outer short-wave surf zone, the interactions gain in strength (Figs. 6b,c). The negative values at B(0.86, 0.04) cause the slight shift of energy around the first harmonic as seen in Fig. 5 (at, e.g., x = 70 m) to somewhat lower frequencies and a gain at low infragravity frequencies. Within the short-wave surf zone, the nonlinear interactions are seen to generally decrease in strength, although there are some exceptions (Figs. 6d,e). For instance, interactions between the peak and its first harmonic B(0.88, 0.44) transfer energy more strongly to its sum f_3. Interestingly, the imaginary part of the bispectrum shows two other peaks: a negative peak at ≈B(0.36, 0.07) and a positive peak at ≈B(0.45, 0.07), indicating the infragravity wave components act as conduits in interactions that broaden the spectral peak. In addition, interactions between the infragravity waves themselves develop that transfer energy from low to high infragravity frequencies. A few meters from the shoreline, interactions involving short-wave frequencies disappear entirely (Fig. 6f). From here on the bispectrum is dominated by infragravity–infragravity interactions. The intermediate and high energetic conditions $A1$ and $A2$ show

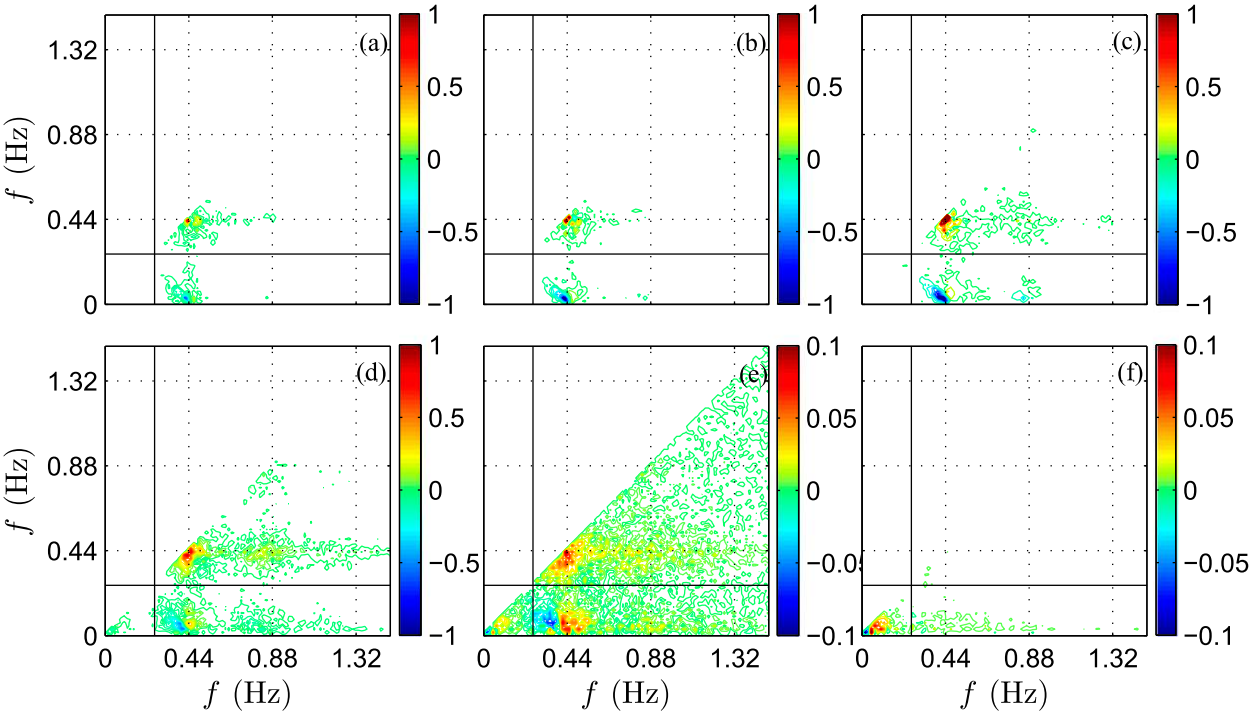

FIG. 6. Imaginary part of the bispectrum ($\times 10^{-8}$) of the incoming wave signal (η^+) at six cross-shore locations for case $A3$ for values where $b^2 > b_{95\%}$. (a) $x = 25.2$ m, (b) $x = 43.3$ m, (c) $x = 58.9$ m, (d) $x = 70.0$ m, (e) $x = 75.2$ m, and (f) $x = 79.2$ m. Black solid lines indicate the cutoff between infragravity and short-wave frequencies f_{IG}. Dashed lines indicate the spectral peak (0.44 Hz) and its higher harmonics.

similar trends (not shown) in bispectral evolution as shown for narrowband condition $A3$ in Fig. 6, although with the broader band spectra, interactions are generally weaker and spread over more frequencies. Furthermore, bispectral values for the high energy condition $A2$ are seen to be considerably stronger than for lower energy condition $A1$, confirming previous studies by, for example, Elgar and Guza (1985) and Norheim et al. (1998).

The integrated short-wave biphases β_{SW} for cases $A1$, $A2$, and $A3$ all evolve from about zero in the shoaling zone, indicative of a skewed wave, to a more sawtooth shaped wave, with $\beta_{SW} \approx -50°$ about 5 m from the shoreline (Fig. 7c). When β_{SW} are calculated using the total rather than incoming wave signal (not shown), which allows us to look closer to the shoreline, β_{SW} is seen to evolve further to a value of $-75°$. The largest shape transformations take place in the short-wave surf zone. The term β_{SW} of high energetic case $A2$ starts to evolve at a location farther offshore because of the larger waves that break farther offshore than during the other two cases. The integrated infragravity/short-wave biphases $\beta_{IG,SW}$, calculated for the incoming wave signal, evolve from $\approx 180°$ (indicative of bound infragravity waves) offshore to $\approx -90°$ close to shore (Fig. 7b). The gradual decrease of $\beta_{IG,SW}$ from 180° to about 140° in the shoaling zone corresponds to field and laboratory observations, as well as theoretical considerations, of a slightly larger phase lag of the infragravity wave behind the short-wave group (e.g., Van Dongeren and Svendsen 1997; Janssen et al. 2003). This phase lag is necessary for energy transfer from the short waves to the infragravity wave frequencies to occur and allows the infragravity waves to grow in height, with a larger phase lag allowing for stronger transfers. The sudden shifts seen in $\beta_{IG,SW}$ from about 140° to $-50°$ are a few meters into the short-wave surf zones where the significant short-wave height (Fig. 2) starts to decrease considerably. Here, the group structure disappears and the coupling of the infragravity waves with the short-wave group disappears too, as seen in De Bakker et al. (2013) for the same dataset and reported for other datasets (e.g., Janssen et al. 2003; Battjes et al. 2004; Van Dongeren et al. 2007). The integrated infragravity biphases β_{IG}, calculated for the incoming wave signal, also evolve from $\approx 180°$ to about $-90°$ (Fig. 7a), except for case $A1$ where β_{IG} evolves only to about $-20°$. The values of $-90°$ indicate a sawtooth shape of the infragravity wave in shallow water, reported earlier for this laboratory dataset by Rocha et al. (2013).

The nonlinear energy transfers S_{nl} including sum and difference interactions for case $A3$ are shown in Fig. 8 as a function of frequency and cross-shore distance. The four panels show transfers by triad interactions involving

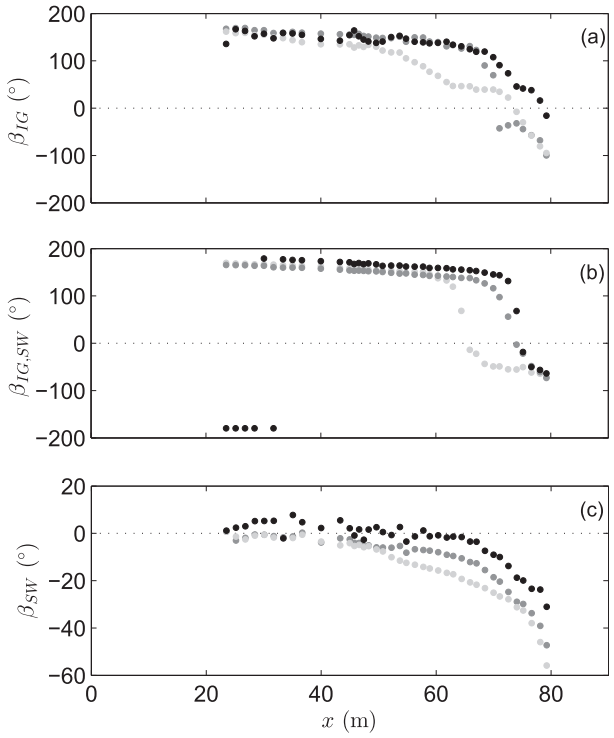

FIG. 7. Biphases determined for the incoming wave signal of wave condition $A1$ (black dots), $A2$ (light gray dots), and $A3$ (dark gray dots) for values where $b^2 > b_{95\%}$ for (a) infragravity, (b) infragravity and short-wave frequencies, and (c) the short-wave frequencies.

either one, two, or three infragravity frequency components or interactions involving only short-wave frequencies (as defined in appendix B). The strongest interactions in the spectrum are the interactions between short-wave frequencies alone ($S_{\mathrm{nl,IV}}$; Fig. 8d). The spectral peak loses energy along the entire flume, which is transferred mainly to its higher harmonics. At the edge of the short-wave surf zone, the first harmonic starts to lose energy, and slightly farther shoreward, the second harmonic loses energy as well. The energy lost by the spectral peak and its harmonics are received by a broad band of high frequencies ($f > 1.5$ Hz) consistent with Herbers et al. (2000) and Smit et al. (2014). Close to shore ($x > 75$ m), the interactions involving short-wave frequencies become very weak, probably caused by the strong energy decay at short-wave frequencies in these depths (Fig. 5). The strength of the interactions between one infragravity and two short-wave frequencies ($S_{\mathrm{nl,III}}$; Fig. 8c) is slightly smaller than $S_{\mathrm{nl,IV}}$. The term $S_{\mathrm{nl,III}}$ represents the classic infragravity interactions where two short-wave frequencies force a third low frequency, here predominantly at $f \approx 0.04$ Hz. The slight shift of the energy around the spectral peak and its harmonics to lower frequencies as seen in Fig. 5 can be understood more clearly with the use of this figure. Energy at frequencies slightly higher than the spectral peak transfer energy to frequencies slightly lower than the spectral peak. This trend is similar for harmonics of the spectral peak. In the short-wave surf zone, energy is seen to be transferred to the spectral valleys. The energy transfer to infragravity frequencies continues until $x \approx 75$ m, from whereon the infragravity frequencies lose energy. Subharmonic interactions between two infragravity frequencies and one short-wave frequency ($S_{\mathrm{nl,II}}$; Fig. 8b) are an order of magnitude smaller than interactions including two or more short-wave frequencies ($S_{\mathrm{nl,III}}$ and $S_{\mathrm{nl,IV}}$). Transfers go from short-wave frequencies to infragravity frequencies until $x \approx 80$ m, where the transfers reverse and higher frequencies receive energy at the expense of the infragravity wave band. Interactions between infragravity frequencies alone start to play a role in the short-wave surf zone (Fig. 8a), and especially from $x \approx 75$ m onward, the interactions grow in strength. A net transfer is directed from the lower infragravity frequencies ($f < 0.15$ Hz) to the higher infragravity frequencies ($f = 0.15$–0.26 Hz) by sum interactions.

Figure 9 compares the nonlinear source term contributions of the three types of interactions including infragravity frequencies ($S_{\mathrm{nl,I}}$, $S_{\mathrm{nl,II}}$, and $S_{\mathrm{nl,III}}$) at four selected locations. At $x = 70.4$ m, interactions are still dominated by the short-wave frequencies $S_{\mathrm{nl,III}}$, from which the infragravity frequencies receive their energy. At $x = 75.2$ m, infragravity frequencies now lose energy by $S_{\mathrm{nl,III}}$ interactions, but at the same time receive energy by $S_{\mathrm{nl,II}}$ interactions. Even closer to shore, at $x = 80.3$ m, triad interactions between infragravity waves alone ($S_{\mathrm{nl,I}}$) become relatively important. A few meters from the shoreline, at $x = 81.5$ m, those transfer patterns increase in strength. The transfers of infragravity energy to higher frequencies in the surf zone suggest that the infragravity waves, as they become dominant, become nonlinear and develop harmonics similar to the short-wave transformation through the surf zone.

4. Discussion

Our results have offered detailed insight into the nonlinear interactions within an irregular wave field as it propagates over a plane-sloping laboratory beach. In this section, we will examine what part of the total energy flux gradient can be explained by nonlinear energy transfers and what part might otherwise be because of dissipation by breaking or frictional losses. In this context, we also address infragravity wave dissipation. Furthermore, we will discuss similarities of the present laboratory findings with field data recently obtained on a gently sloping beach (De Bakker et al. 2014).

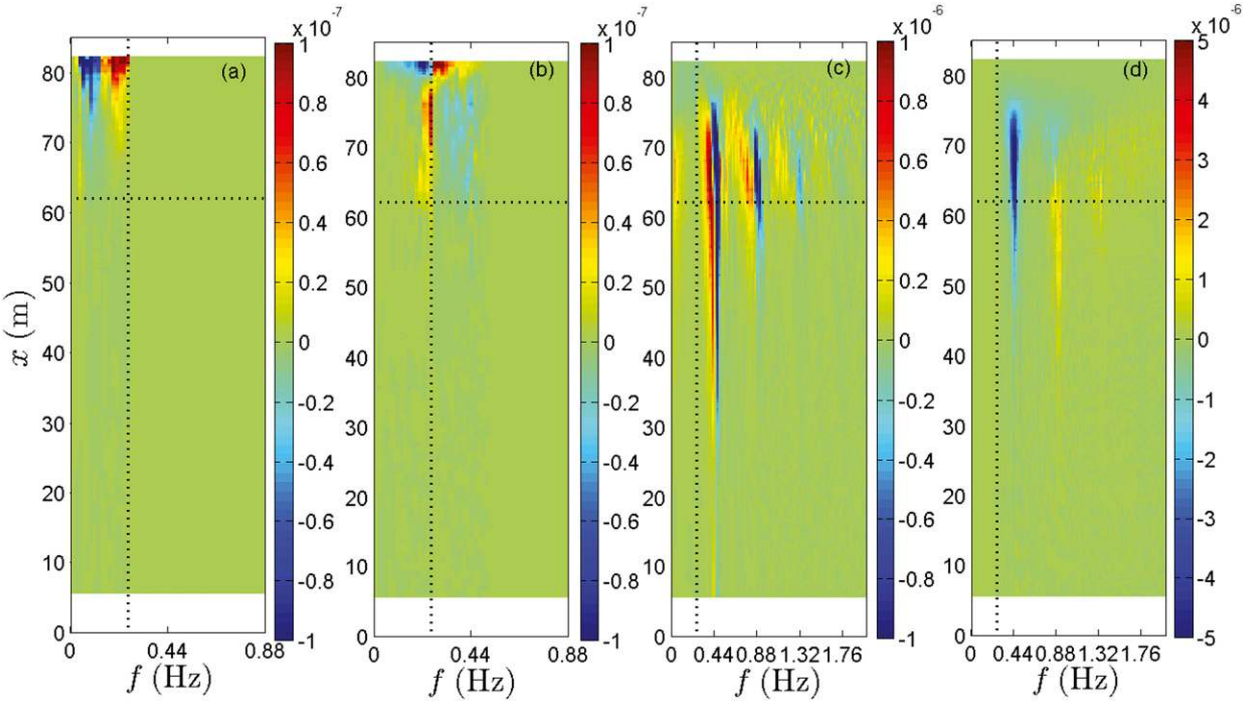

FIG. 8. Nonlinear source term S_{nl} estimated from the total wave signal of irregular wave condition *A*3 plotted vs frequency f and cross-shore position x. With (a) infragravity frequencies only ($S_{nl,I}$), (b) two infragravity frequencies and one short-wave frequency ($S_{nl,II}$), (c) two short-wave frequencies and one infragravity frequency ($S_{nl,III}$), and (d) short-wave frequencies only ($S_{nl,IV}$). The horizontal dashed line indicates the start of the short-wave surf zone. The vertical dashed line indicates the cutoff between infragravity and sea–swell frequencies. Note the different x axis and the different color scaling for (a) and (b) vs (c) and (d).

a. Energy transport equation

Figure 10 displays the energy flux gradient (Fig. 10a) and the nonlinear source term (Fig. 10b) versus the frequency and cross-shore position and compares the estimates at three locations close to and in the short-wave surf zone (Figs. 10c–e). As can be seen, a large part of the variation in F_x is explained by S_{nl}. The energy losses at the spectral peak, and the energy gain (Fig. 10c) and subsequent loss (Fig. 10d) at the first harmonic, are because of nonlinear energy transfers. Even close to the shoreline, S_{nl} accounts largely for the trends seen in F_x (Fig. 10e), although for $f < 0.1$ Hz reflection disturbs the F_x signal considerably. The large gain of energy at high frequencies in the short-wave surf zone seen in S_{nl} is not present in F_x, a trend reported before by Herbers et al. (2000) and Smit et al. (2014). Apparently, energy is transferred to higher frequencies where the energy is then dissipated, instead of direct dissipation in the energetic part of the spectrum. This indicates that the decay of wave spectra in the surf zone is primarily the result of nonlinear energy transfers to higher frequencies and that the actual dissipation occurs in the high-frequency tail of the spectrum (Herbers et al. 2000).

Figure 11a shows the comparison of S_{nl} and F_x for infragravity frequencies integrated over $f = 0.1$–0.26 Hz. The infragravity wave energy gain throughout the shoaling zone and energy loss close to the shoreline are explained almost completely by the nonlinear energy transfers. However, in between $x \approx 62$ m and $x \approx 75$ m, the outer region of the short-wave surf zone, S_{nl} and F_x differ noticeably. A similar mismatch is observed in the exact same region, when looking at the frequency-integrated terms for the peak frequency ($0.38 < f < 0.50$ Hz) (Fig. 11b). Although other processes might be relevant, it seems likely that the abrupt wave transformation and subsequent energy exchanges are not described completely by the applied second-order Boussinesq approximation and that errors in S_{nl} are the main source of the $S_{nl} - F_x$ mismatch. To describe the processes in this energetic part of the surf zone, and especially at frequencies larger than the first harmonic where $kh > 1$, third- and higher-order interactions likely need to be incorporated. A similar mismatch was identified in Thomson et al. (2006), who used the same interaction coefficient to determine nonlinear energy transfers to and from infragravity waves. Although some mismatch exists in the short-wave surf zone, overall the energy losses at both infragravity and short-wave frequencies can largely be

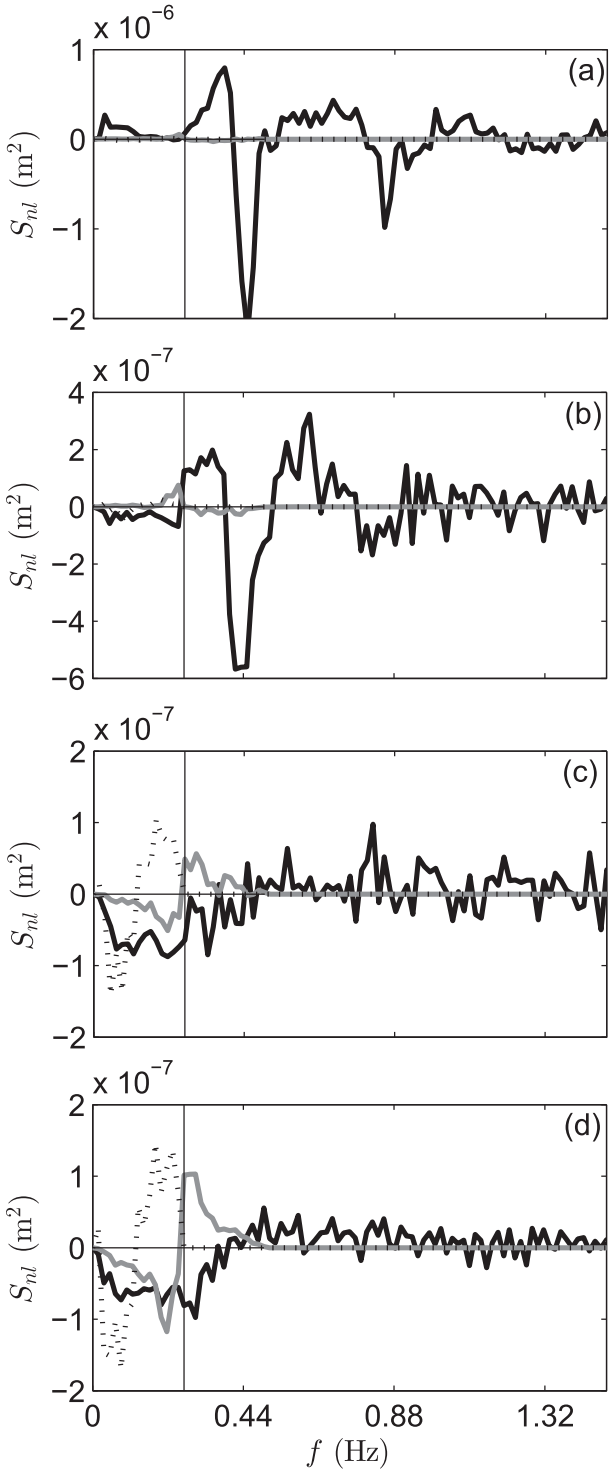

FIG. 9. Nonlinear source term S_{nl} estimated from the total wave signal of irregular wave condition *A*3 vs frequency f at four cross-shore locations at (a) $x = 70.4$ m, (b) $x = 75.2$ m, (c) $x = 80.3$ m, and (d) $x = 81.5$ m. The source term estimates are separated into contributions from triad interactions including either infragravity frequencies only ($S_{nl,I}$, dashed), two infragravity frequencies and one short-wave frequency ($S_{nl,II}$, gray), or two short-wave frequencies and one infragravity frequency ($S_{nl,III}$, black). The vertical line indicates the cutoff between infragravity and short-wave frequencies f_{IG}. Note the different y-axes scales for the subplots.

explained by a cascade of nonlinear energy transfers to the very high frequencies. At these high frequencies, the energy is then dissipated.

Intriguingly, neither the observed bispectra (Fig. 6) nor the deduced energy exchanges (Figs. 8 and 9) indicate a considerable transfer from infragravity to short-wave frequencies. This contrasts with the findings of Henderson et al. (2006) who identified energy gain at the peak frequency through interactions with infragravity frequencies. It is important to note that we observe the dominant reduction in infragravity wave height to take place shoreward of our most landward used sensor (Figs. 2d–f), where we have seen infragravity waves dominate the power spectrum and infragravity–infragravity interactions dominate the bispectrum. Infragravity frequencies dominate the swash energy spectrum as well in the present data (Ruju et al. 2014). The infragravity–infragravity interactions induce higher harmonics that allow for the shape transformation of the infragravity waves. This then leads to the steepening and asymmetric shape of the infragravity wave (see Fig. 7a) and eventually to breaking. These findings might indicate the presence of an infragravity wave surf zone inshore of the short-wave surf zone.

b. *Field data*

With the absence of directional spread in the laboratory data, the ratio of infragravity to short-wave energy is likely to be considerably larger than in the field (e.g., Herbers et al. 1995). To investigate whether the relatively large importance of infragravity energy in the laboratory data alters bispectral trends, we compare our one-directional laboratory observations with the field observations of De Bakker et al. (2014). Bispectra were calculated for an intermediate energy condition (offshore $H_s = 1.5$ m, $T_p = 4.8$ s, and incidence wave angle $\theta = 21.2°$) measured during a high tide on a 1:80 beach, located on the barrier island Ameland, the Netherlands (Ruessink et al. 2012). For the bispectral analysis, the time series (sampled at 4 Hz) were processed in blocks of 15 min (total record length was 120 min). Averaging of the bispectral estimates over seven frequencies resulted in a frequency resolution of 0.0078 Hz and 210 degrees of freedom. The b^2 values over 0.169 are statistically significant from 0 at the 95% confidence level, based on the approximation of Kim and Powers (1979).

Figure 12 shows power spectra of two locations in the surf zone, with one location that is dominated by short-wave frequencies (local spectral peak at $f = 0.09$ Hz, $h = 1.64$ m) and one location in shallower water, where infragravity waves dominate ($f < 0.05$ Hz, $h = 0.97$ m). Figure 13 shows the accompanying bispectra. From Fig. 13a, we infer that the spectral peak transfers energy

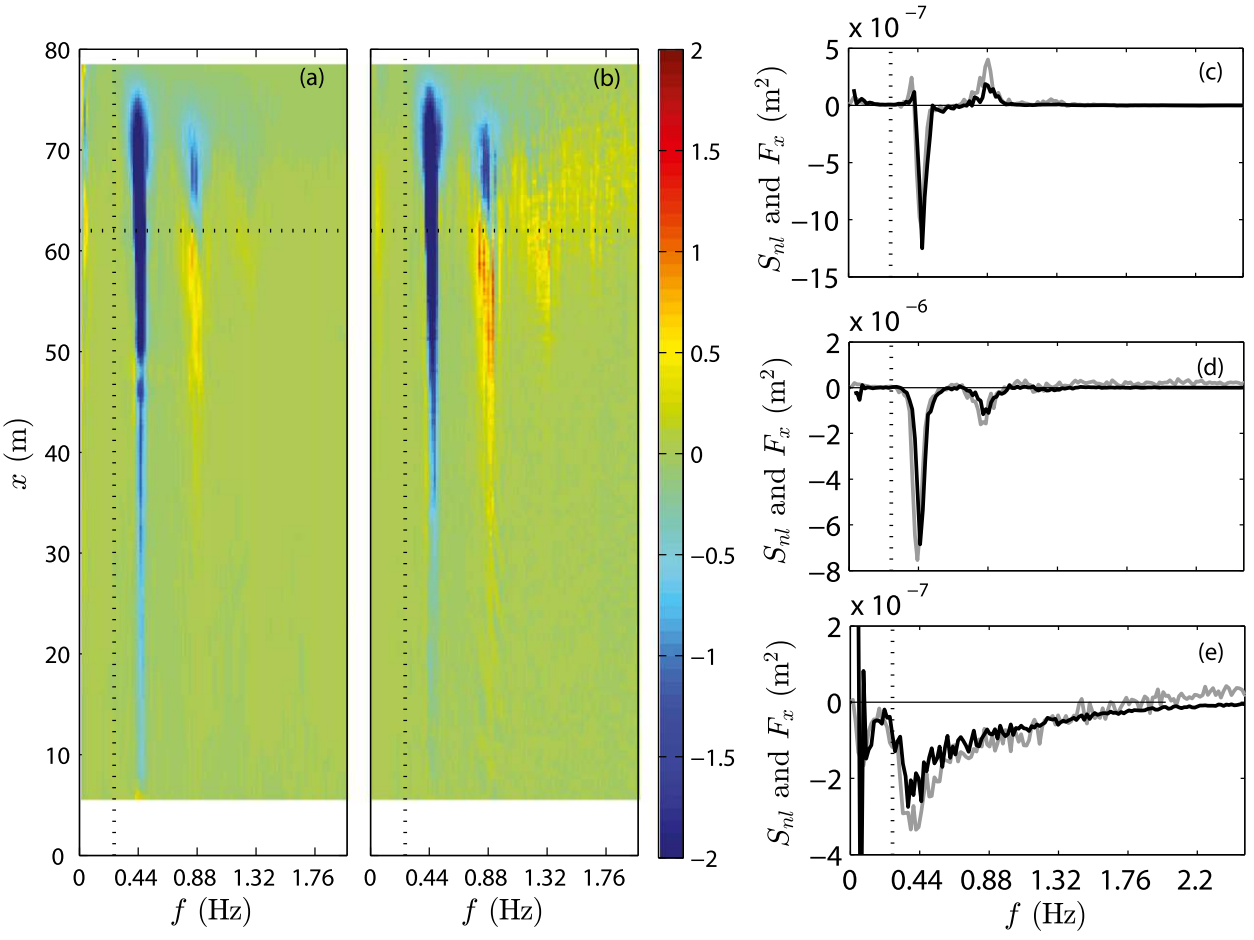

FIG. 10. (a) Energy flux gradients F_x ($\times 10^{-6}$) and (b) nonlinear source term S_{nl} ($\times 10^{-6}$) as a function of frequency f and cross-shore distance x estimated from the total wave signal of swell case $A3$. The horizontal dashed line indicates the start of the short-wave surf zone. The vertical dashed line indicates the cutoff between infragravity frequencies and short-wave frequencies. The term F_x (black) compared with S_{nl} (gray) at (c) $x = 58.9$ m, (d) $x = 70.0$ m, and (e) $x = 79.2$ m.

to the first harmonic, judging from positive interaction at $B(0.09, 0.09)$. The negative interactions at, for example, $B(0.09, 0.03)$ and $B(0.045, 0.04)$ show energy transfers from the short-wave frequencies to infragravity frequencies. Figure 13b shows that interactions at infragravity frequencies dominate close to shore ($h < 0.97$ m), and interactions involving short-wave frequencies have disappeared, consistent with our laboratory observations.

Overall, our laboratory results for three irregular wave fields progressing over a gently sloping laboratory beach, and the Ameland field observations, all show that dominant wave interactions close to shore are among infragravity frequencies, and the infragravity motions are largely dissipated near the shoreline with very little reflection. These results differ from the infragravity wave evolution observed on steeper beaches (Elgar et al. 1994; Henderson et al. 2006; Thomson et al. 2006) that is characterized by strong shoreline reflection and energy transfers back to the incident short waves. Additional data collection and numerical modeling are necessary to investigate the effect of the beach slope and beach shape on the strength of nonlinear interactions involving infragravity waves. The presence of a sandbar might, as suggested by Norheim et al. (1998), for instance force a different trend in the exchange of energy.

5. Conclusions

Using a high-resolution laboratory dataset, we explored nonlinear energy transfers within an irregular wave field as it progresses over a gently sloping (1:80) beach. In the shoaling zone, the nonlinear interactions are dominated by sum interactions transferring energy from the spectral peak to its higher harmonics and by difference interactions creating infragravity energy. While receiving net energy, infragravity waves simultaneously participate in sum and difference interactions

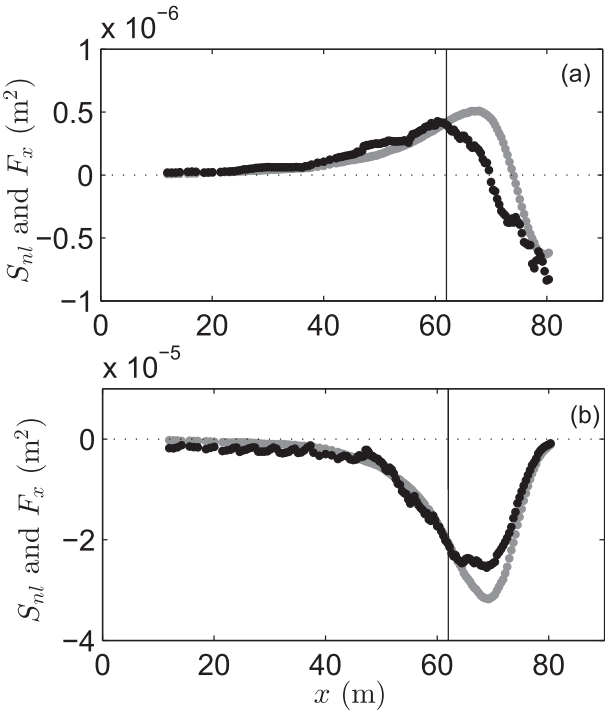

FIG. 11. (a) Energy flux gradients F_x ($\times 10^{-6}$) (black dots) and (b) nonlinear source term S_{nl} ($\times 10^{-6}$) (gray dots) integrated for (a) the higher infragravity frequencies (0.10–0.26 Hz) and (b) the offshore spectral peak frequency (0.38–0.50 Hz) vs cross-shore distance x. The vertical black line indicates the start of the short-wave surf zone.

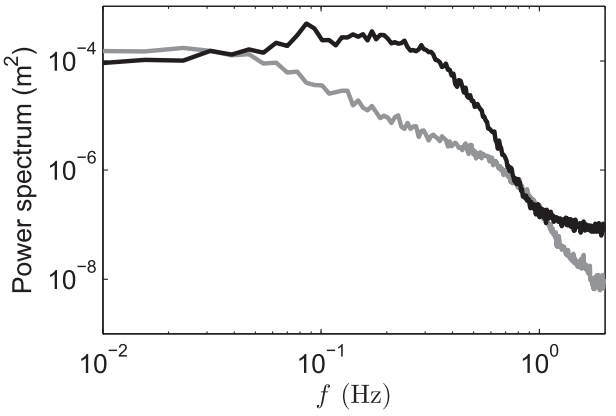

FIG. 12. Power spectrum of a moderate energy wave field at high tide in water depths of $h = 1.64$ m (black) and $h = 0.97$ m (gray) during the Ameland campaign in 2010.

that spread energy of the short-wave peaks to adjacent frequencies, thereby creating a broader energy spectrum. In the short-wave surf zone, infragravity–infragravity interactions develop that transfer energy from low infragravity frequencies to high infragravity frequencies. Close to shore, where almost no short-wave energy remains, the interactions are dominated by these infragravity frequencies. Overall, the nonlinear energy transfers balance with the gradient in the energy flux, although a mismatch exists in the outer short-wave surf zone, probably because of the Boussinesq approximation that does not take higher-order interactions into account, while the wave field is highly nonlinear. Instead of dissipation at the infragravity and short-wave frequencies directly, the energy cascades to higher frequencies ($f > 1.5$ Hz) where it presumably dissipates. The largest decrease in infragravity wave height close to the shoreline, where infragravity–infragravity interactions dominate and force the transformation of the infragravity wave shape to asymmetric, suggest

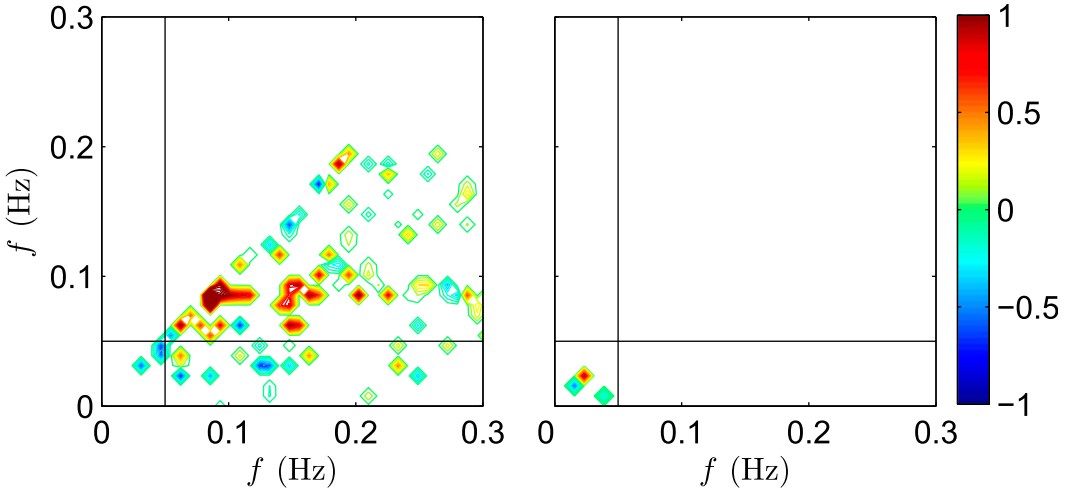

FIG. 13. Imaginary part of the bispectrum ($\times 10^{-6}$) of a moderate energy wave field at high tide, for values where $b^2 > b_{95\%}$, in water depths of (left) $h = 1.64$ m and (right) $h = 0.97$ m during the Ameland campaign in 2010. Black lines indicate the cutoff from infragravity frequencies ($f < 0.05$ Hz) to sea–swell frequencies ($f > 0.05$ Hz).

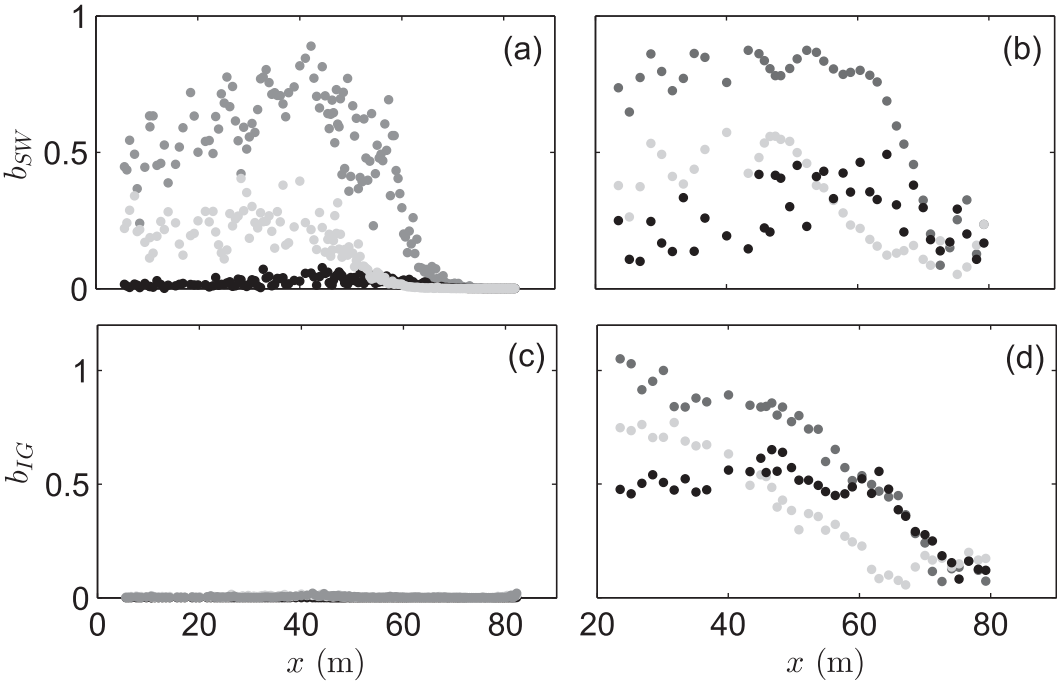

FIG. A1. Bicoherence determined for the (left) total (η) and (right) incoming (η^+) wave signal of wave condition $A1$ (black dots), $A2$ (light gray dots), and $A3$ (dark gray dots). (a),(b) At the offshore spectral peak frequency (f = 0.63 Hz for case $A1$ and f = 0.44 Hz for cases $A2$ and $A3$). (c),(d) At the dominant infragravity frequency (f = 0.04 Hz).

infragravity wave breaking to be the dominant mechanism of infragravity wave dissipation.

Acknowledgments. The GLOBEX project was coordinated by Hervé Michallet (LEGI, Université de Grenoble) and Gerben Ruessink (Utrecht University) and supported by the European Community's Seventh Framework Programme through the Hydralab IV project, EC Contract 261520. The authors thank all fellow researchers and Deltares employees involved in the project. T. H. C. Herbers is supported by the Office of Naval Research Littoral Geosciences and Optics Program. This work was funded by the Netherlands Organisation for Scientific Research (NWO) under Contract 821.01.012.

APPENDIX A

Total versus Incoming Wave Signal

Although the bulk infragravity wave reflection from the shoreline is low for all three irregular wave cases ($R^2 \approx 0.1$; Figs. 3d–f), the outgoing infragravity waves may considerably disturb the observed frequency coupling and hence the bispectral signal (e.g., Elgar and Guza 1985). Using only the incoming wave signal would therefore result in more accurate analysis, but the downside is the limited number of available locations because of the needed collocated wave gauge and velocity meters to separate the incoming and outgoing signals (see section 2b). Here, we compare bicoherence and bispectral values of the incoming (η^+) and total (η) wave signals to examine the sensitivity of bispectra and nonlinear source term estimates to the exclusion of reflected waves.

Figure A1 shows bicoherence values for the total wave signals of cases $A1$, $A2$, and $A3$ for the offshore spectral peak frequency (Fig. A1a) and the dominant infragravity frequency of 0.04 Hz (Fig. A1c), providing a normalization for the coupling strength between frequencies. Bicoherence values for the offshore spectral peak are highest for case $A3$ because of the narrow-banded shape of the spectrum that enhances strong coupling between specific frequencies. For all three cases, b^2 for the offshore spectral peak are seen to decrease slightly in the shoaling zone, but the strongest decrease takes place in the short-wave surf zone where the coupling decreases strongly because of breaking and where bicoherence values are limited to 0.2. The bicoherence b^2 for the dominant infragravity frequency is very low, with values < 0.05. Although case $A2$ has a considerably higher wave height that would promote

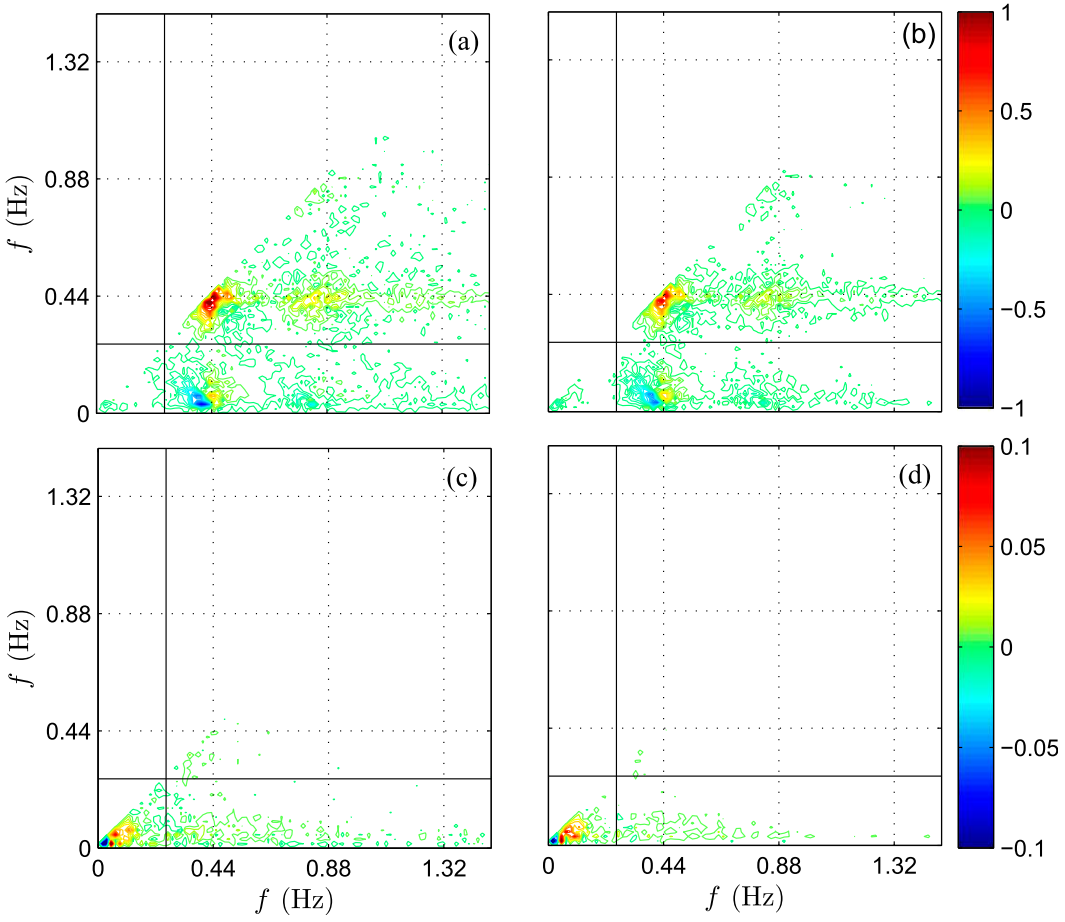

FIG. A2. Imaginary part of the bispectra ($\times 10^{-8}$) of wave condition *A*3 for the (a) total wave signal η at $x = 70.0$ m, (b) incoming wave signal η^+ at $x = 70.0$ m, (c) total wave signal η at $x = 79.2$ m, and (d) incoming wave signal η^+ at $x = 79.2$ m.

larger bispectral values, the broadbanded shape of the spectrum reduces the coupling strength. Case *A*1 has the weakest bicoherence values, due to both the moderately high waves and the broadbanded spectral shape. When bicoherence values are determined for the incoming wave signal, values increase considerably, especially for the dominant infragravity frequency (Figs. A1b,d), indicating that the waves reflected from the shore might indeed disturb the bispectral signal, especially for the infragravity wave frequencies.

As bispectral values for infragravity frequencies are very small in deep water, bicoherence levels are not that informative in this region. A comparison of the imaginary part of the bispectrum for *A*3 at a location in the surf zone ($x = 70.0$ m; Figs. A2a,b), where bicoherence values reach up to ≈0.2 shows that although the bispectral values for η^+ are slightly smaller than for η, the trends are very similar. Interactions within the spectral peak are also slightly influenced by the separation method. Bispectral values for η^+ and η at a few meters from the shoreline ($x = 79.2$ m; Figs. A2c,d), where infragravity frequencies dominate, show very similar trends as well, indicating that although reflected waves alter the bicoherence values, the bispectral signal is not altered considerably, not even at infragravity frequencies.

APPENDIX B

Separated S_{nl} Terms

The nonlinear source term $S_{nl,f}$ represents the net transfer of energy to (or from) waves with frequency f through triad interactions. It is often convenient to express the integral of S_{nl} in the terms of an integration over the positive quadrant of the bispectrum alone or equivalently in terms of the sum and difference interactions:

TABLE B1. Definition of the set of f' over which the summation of the sum interactions is taken.

Set	Defined such that	If
F_{I}^{+}	$0 < f' \le f$	$0 < f \le f_{\mathrm{IG}}$
	0	Elsewhere
F_{II}^{+}	$f - f_{\mathrm{IG}} < f' \le f_{\mathrm{IG}}$	$f_{\mathrm{IG}} < f \le 2f_{\mathrm{IG}}$
	0	Elsewhere
F_{III}^{+}	$0 < f' \le f - f_{\mathrm{IG}}$ or $f_{\mathrm{IG}} < f' \le f$	$f_{\mathrm{IG}} < f \le 2f_{\mathrm{IG}}$
	$0 < f' \le f_{\mathrm{IG}}$ or $f - f_{\mathrm{IG}} < f' \le f$	$2f_{\mathrm{IG}} < f \le f_N$
	0	Elsewhere
F_{IV}^{+}	$f_{\mathrm{IG}} < f' \le f - f_{\mathrm{IG}}$	$2f_{\mathrm{IG}} < f \le f_N$
	0	Elsewhere

TABLE B2. Definition of the set of f' over which the summation of the difference interactions is taken.

Set	Defined such that	If
F_{I}^{-}	$0 < f' \le f_{\mathrm{IG}} - f$	$0 < f \le f_{\mathrm{IG}}$
	0	Elsewhere
F_{II}^{-}	$f_{\mathrm{IG}} - f < f' \le f_{\mathrm{IG}}$	$0 < f \le f_{\mathrm{IG}}$
	0	Elsewhere
F_{III}^{-}	$f_{\mathrm{IG}} < f' \le f_N - f$	$0 < f \le f_{\mathrm{IG}}$
	$0 < f' \le \min(f_N - f, f_{\mathrm{IG}})$	$f_{\mathrm{IG}} < f \le f_N$
	0	Elsewhere
F_{IV}^{-}	$f_{\mathrm{IG}} < f' \le f_N - f$	$f_{\mathrm{IG}} < f \le f_N - f_{\mathrm{IG}}$
	0	Elsewhere

$$S_{\mathrm{nl},f} = S_{\mathrm{nl},f}^{+} + S_{\mathrm{nl},f}^{-}, \tag{B.1}$$

where the sum and difference contributions are expressed as

$$S_{\mathrm{nl},f}^{+} = \sum_{f' \in F^{+}} W_{f',f-f'} \, \mathrm{Im}\{B_{f',f-f'}\}, \tag{B.2}$$

and

$$S_{\mathrm{nl},f}^{-} = -2 \sum_{f' \in F^{-}} W_{f+f',-f'} \, \mathrm{Im}\{B_{f,f'}\}, \tag{B.3}$$

respectively, where in case of the Boussinesq scaling, $W(f_1, f_2) = [3\pi(f_1 + f_2)]/h$. The sum contributions are obtained by integrating diagonally over the bispectrum, and the difference contributions are obtained by integrating along straight lines perpendicular to the x and y axes (see dashed gray lines in Fig. 4).

To obtain more insight in nonlinear interactions involving infragravity frequencies, we separate the integrals over the bispectrum into four different zones as depicted in Fig. 4. The terms $S_{\mathrm{nl},f}^{+}$ and $S_{\mathrm{nl},f}^{-}$ are rewritten as

$$S_{\mathrm{nl},f}^{\pm} = S_{\mathrm{nl},f,\mathrm{I}}^{\pm} + S_{\mathrm{nl},f,\mathrm{II}}^{\pm} + S_{\mathrm{nl},f,\mathrm{III}}^{\pm} + S_{\mathrm{nl},f,\mathrm{IV}}^{\pm}, \tag{B.4}$$

where $S_{\mathrm{nl},f,\mathrm{I}}$ describes interactions with only infragravity frequencies involved, $S_{\mathrm{nl},f,\mathrm{II}}$ describes interactions between two infragravity and one short-wave frequency, $S_{\mathrm{nl},f,\mathrm{III}}$ describes interactions between two short-wave and one infragravity frequency, and $S_{\mathrm{nl},f,\mathrm{IV}}$ describes interactions between short-wave frequencies alone. Note that when using the Boussinesq coefficient, just as the total term, all the terms separately are conservative; that is, the integral over the combined sum and difference interactions applying to a specific zone is zero. The set of f' over which the summation is taken is defined using the infragravity separation frequency f_{IG} and the Nyquist frequency $f_N = 5$ Hz and is specified per zone in Table B1 for the sum interactions and in Table B2 for the difference interactions.

REFERENCES

Battjes, J. A., H. J. Bakkenes, T. T. Janssen, and A. R. van Dongeren, 2004: Shoaling of subharmonic gravity waves. *J. Geophys. Res.,* **109,** C02009, doi:10.1029/2003JC001863.

Collis, W., P. White, and J. Hammond, 1998: Higher-order spectra: The bispectrum and trispectrum. *Mech. Syst. Signal Process.,* **12,** 375–394, doi:10.1006/mssp.1997.0145.

De Bakker, A., M. Tissier, V. Marieu, N. Sénéchal, A. Ruju, J. Lara, and B. G. Ruessink, 2013: Infragravity wave propagation and dissipation on a low-sloping laboratory beach. *Proc. Seventh Int. Conf. on Coastal Dynamics,* Bordeaux, France, Bordeaux University, 443–452. [Available online at http://www.coastaldynamics2013.fr/pdf_files/040_de_Bakker_Anouk_p.pdf.]

——, ——, and B. G. Ruessink, 2014: Shoreline dissipation of infragravity waves. *Cont. Shelf Res.,* **72,** 73–82, doi:10.1016/j.csr.2013.11.013.

Elgar, S., and R. T. Guza, 1985: Observations of bispectra of shoaling surface gravity waves. *J. Fluid Mech.,* **161,** 425–448, doi:10.1017/S0022112085003007.

——, T. H. C. Herbers, and R. T. Guza, 1994: Reflection of ocean surface gravity waves from a natural beach. *J. Phys. Oceanogr.,* **24,** 1503–1511, doi:10.1175/1520-0485(1994)024<1503:ROOSGW>2.0.CO;2.

Guedes, M., K. R. Bryan, and G. Coco, 2013: Observations of wave energy fluxes and swash motions on a low-sloping, dissipative beach. *J. Geophys. Res. Oceans,* **118,** 3651–3669, doi:10.1002/jgrc.20267.

Guza, R. T., and E. B. Thornton, 1982: Observations of surf beat. *J. Geophys. Res.,* **87,** 483–491, doi:10.1029/JC087iC01p00483.

——, ——, and R. A. Holman, 1984: Swash on steep and shallow beaches. *Proc. 19th Int. Conf. on Coastal Engineering,* Houston, TX, ASCE, 708–723. [Available online at https://icce-ojs-tamu.tdl.org/icce/index.php/icce/article/view/3829.]

Hasselmann, K., W. Munk, and G. MacDonald, 1963: Bispectra of ocean waves. *Proceedings of the Symposium on Time Series Analysis,* M. Rosenblatt, Ed., Vol. 7, John Wiley, 125–139.

Henderson, S. M., R. T. Guza, S. Elgar, T. H. C. Herbers, and A. J. Bowen, 2006: Nonlinear generation and loss of infragravity wave energy. *J. Geophys. Res.,* **111,** C12007, doi:10.1029/2006JC003539.

Herbers, T. H. C., and M. C. Burton, 1997: Nonlinear shoaling of directionally spread waves on a beach. *J. Geophys. Res.,* **102,** 21 101–21 114, doi:10.1029/97JC01581.

——, S. Elgar, and R. T. Guza, 1994: Infragravity-frequency (0.005–0.05 Hz) motions on the shelf. Part I: Forced waves. *J. Phys. Oceanogr.,* **24,** 917–927, doi:10.1175/1520-0485(1994)024<0917:IFHMOT>2.0.CO;2.

——, ——, and R. Guza, 1995: Generation and propagation of infragravity waves. *J. Geophys. Res.,* **100,** 24 863–24 872, doi:10.1029/95JC02680.

——, N. R. Russnogle, and S. Elgar, 2000: Spectral energy balance of breaking waves within the surf zone. *J. Phys. Oceanogr.,* **30,** 2723–2737, doi:10.1175/1520-0485(2000)030<2723:SEBOBW>2.0.CO;2.

Janssen, T. T., 2006: Nonlinear surface waves over topography. Ph.D. thesis, Technical University of Delft, 223 pp.

——, J. A. Battjes, and A. R. van Dongeren, 2003: Long waves induced by short-wave groups over a sloping bottom. *J. Geophys. Res.,* **108,** 3252, doi:10.1029/2002JC001515.

Kim, Y., and E. Powers, 1979: Digital bispectral analysis and its application to nonlinear wave interactions. *IEEE Trans. Plasma Sci.,* **7,** 120–131, doi:10.1109/TPS.1979.4317207.

Lin, Y. H., and H. H. Hwung, 2012: Infra-gravity wave generation by the shoaling wave groups over beaches. *China Ocean Eng.,* **26,** 1–18, doi:10.1007/s13344-012-0001-9.

Longuet-Higgins, M. S., and R. W. Stewart, 1962: Radiation stress and mass transport in gravity waves, with application to 'surf beats.' *J. Fluid Mech.,* **13,** 481–504, doi:10.1017/S0022112062000877.

Norheim, C., T. Herbers, and S. Elgar, 1998: Nonlinear evolution of surface wave spectra on a beach. *J. Phys. Oceanogr.,* **28,** 1534–1551, doi:10.1175/1520-0485(1998)028<1534:NEOSWS>2.0.CO;2.

Rocha, M., H. Michallet, P. Silva, A. Tiago, and E. Bartlemy, 2013: Nonlinearities of short and long waves across the shoaling, surf and swash zones: Physical model results. *Proc. Seventh Int. Conf. on Coastal Dynamics,* Bordeaux, France, Bordeaux University, 1329–1340. [Available online at www.coastaldynamics2013.fr/pdf_files/129_Rocha_mariana.pdf.]

Ruessink, B. G., 1998: Bound and free infragravity waves in the nearshore zone under breaking and nonbreaking conditions. *J. Geophys. Res.,* **103,** 12 795–12 805, doi:10.1029/98JC00893.

——, M. Boers, P. van Geer, A. de Bakker, A. Pieterse, F. Grasso, and R. de Winter, 2012: Towards a process-based model to predict dune erosion along the Dutch Wadden coast. *Neth. J. Geosci.,* **91,** 357–372, doi:10.1017/S0016774600000494.

——, H. Michallet, P. Bonneton, D. Mouaz, J. Lara, P. Silva, and P. Wellens, 2013: Globex: Wave dynamics on a gently sloping laboratory beach. *Proc. Seventh Int. Conf. on Coastal Dynamics,* Bordeaux, France, Bordeaux University, ASCE, 1351–1362. [Available online at www.coastaldynamics2013.fr/pdf_files/131_Ruessink_gerben.pdf.]

Ruju, A., J. Lara, and I. Losada, 2012: Radiation stress and low-frequency energy balance within the surf zone: A numerical approach. *Coastal Eng.,* **68,** 44–55, doi:10.1016/j.coastaleng.2012.05.003.

——, ——, and ——, 2014: Numerical analysis of run-up oscillations under dissipative conditions. *Coastal Eng.,* **86,** 45–56, doi:10.1016/j.coastaleng.2014.01.010.

Russell, P., 1993: Mechanisms for beach erosion during storm. *Cont. Shelf Res.,* **13,** 1243–1265, doi:10.1016/0278-4343(93)90051-X.

Sénéchal, N., G. Coco, K. R. Bryan, and R. A. Holman, 2011: Wave runup during extreme storm conditions. *J. Geophys. Res.,* **116,** C07032, doi:10.1029/2010JC006819.

Sheremet, A., R. T. Guza, S. Elgar, and T. H. C. Herbers, 2002: Observations of nearshore infragravity waves: Seaward and shoreward propagating components. *J. Geophys. Res.,* **107,** doi:10.1029/2001JC000970.

Smit, P., T. Janssen, L. Holthuijsen, and J. Smith, 2014: Non-hydrostatic modeling of surf zone wave dynamics. *Coastal Eng.,* **83,** 36–48, doi:10.1016/j.coastaleng.2013.09.005.

Thomson, J., S. Elgar, B. Raubenheimer, T. H. C. Herbers, and R. T. Guza, 2006: Tidal modulation of infragravity waves via nonlinear energy losses in the surfzone. *Geophys. Res. Lett.,* **33,** L05601, doi:10.1029/2005GL025514.

Thornton, E., 1979: Energetics of breaking waves within the surf zone. *J. Geophys. Res.,* **84,** 4931–4938, doi:10.1029/JC084iC08p04931.

Van Dongeren, A., and I. A. Svendsen, 1997: Quasi 3-D modeling of nearshore hydrodynamics. Center for Applied Coastal Research Tech. Rep., Research Rep. CACR-97-04, 243 pp.

——, J. Battjes, T. Janssen, J. van Noorloos, K. Steenhauer, G. Steenbergen, and A. Reniers, 2007: Shoaling and shoreline dissipation of low-frequency waves. *J. Geophys. Res.,* **112,** C02011, doi:10.1029/2006JC003701.

Van Leeuwen, P. J., and G. Klopman, 1996: A new method for the generation of second-order random waves. *Ocean Eng.,* **23,** 167–192, doi:10.1016/0029-8018(95)00027-5.

Van Thiel de Vries, J. S. M., M. R. A. van Gent, D. J. R. Walstra, and A. J. H. M. Reniers, 2008: Analysis of dune erosion processes in large-scale flume experiments. *Coastal Eng.,* **55,** 1028–1040, doi:10.1016/j.coastaleng.2008.04.004.